3D Reconstruction of Pore and Fracture Structures in Crushed Soft Coal with Low Permeability and Its Permeability Analysis: Implications for the Design of CO_2 Injection and CH_4 Production

Published as part of ACS Omega virtual special issue "CO2 Geostorage".

Jilin Wang,* Huihuang Fang,* Wan Cao, Bicong Wang, and Xinghe Wu

Read Online

ACCESS | Metrics & More | Article Recommendations

ABSTRACT: In order to improve the CO_2 injection and CH_4 production efficiencies during the CO_2-ECBM process, it is necessary to clarify the relationship among the complexity of pore and fracture structures, the typicality of the fluid migration path, and the heterogeneity of reservoir permeability. In this study, crushed soft coal with low permeability from Huainan and Huaibei coalfields of China was taken as the research object. First, the three-dimensional (3D) visualization reconstruction of pore and fracture structures was realized. Second, the equivalent pore and fracture network model was constructed. Finally, the permeability evolution and its anisotropy of the coal reservoir were dynamically demonstrated. In this study, the implication of surface porosity

on the heterogeneity of pore and fracture structures was first discussed, followed by the implication of coordination number on the anisotropy of fluid flow, and finally, the influence of the anisotropy of fluid flow on the CO_2-ECBM process was discussed. The results show that the equivalent pore and fracture network models of the reservoir structure can be constructed based on the digital rock physics technology. The analysis results of porosity, interconnected porosity, typical path of fluid migration, absolute permeability, and surface porosity of each sample have good consistency in characterizing the complexity of pore and fracture structures and the heterogeneity of permeability. The average coordination numbers of RL and LZ samples are 5.99 and 5.78, respectively, and the number of pores and throats is well-balanced, which indicates that LZ and RL collieries are suitable for the development of CO_2-ECBM industrial tests. When the interconnected pores and fractures are mainly developed vertically and horizontally, the construction of drilling technology of the CO_2-ECBM process should be mainly designed for vertical wells and horizontal wells, respectively. This study has important theoretical and practical significance for the industrial testing and commercialization of CO_2-ECBM technology in crushed soft coal with low permeability.
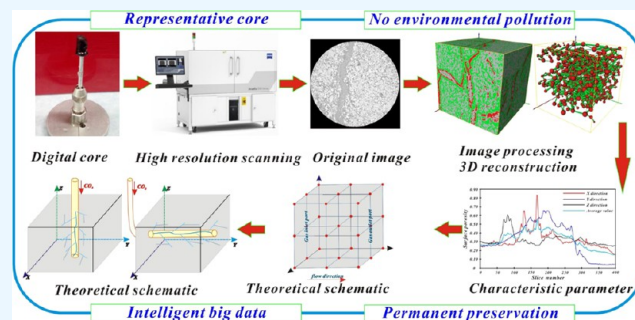
1. INTRODUCTION

The technology of CO_2 injection for CH_4 production (i.e., CO_2-ECBM) makes use of the difference in the adsorption capacity of CH_4 and CO_2 in coal to achieve the effect of CBM production by injecting CO_2 into coal,[1,2] which has the dual benefits of environmental improvement and energy production. The development of an industrial test and its commercialization of CO_2-ECBM technology are mainly affected by the pore and fracture structures and the injection and production technologies of CO_2/CH_4.[3,4] Permeability is not only a direct reflection of the pore and fracture structure and characteristics of coal reservoirs but also a key parameter to characterize the migration and seepage capacity of fluids during the CO_2-ECBM process,[5,6] which has important impacts on CO_2 injection and CH_4 production efficiencies. Therefore, permeability analysis can play good roles in

communication between the pore and fracture structures and the injection and production processes of CO_2/CH_4.

The pore and fracture structures are developed at the nanometer to centimeter scale, which control the adsorption, desorption, diffusion, and seepage processes of a fluid in coal.[7,8] There are two main methods for the observation and analysis of pore and fracture structures in porous media: indirect imaging and direct imaging. Indirect methods include mercury injection, gas adsorption, and nuclear magnetic
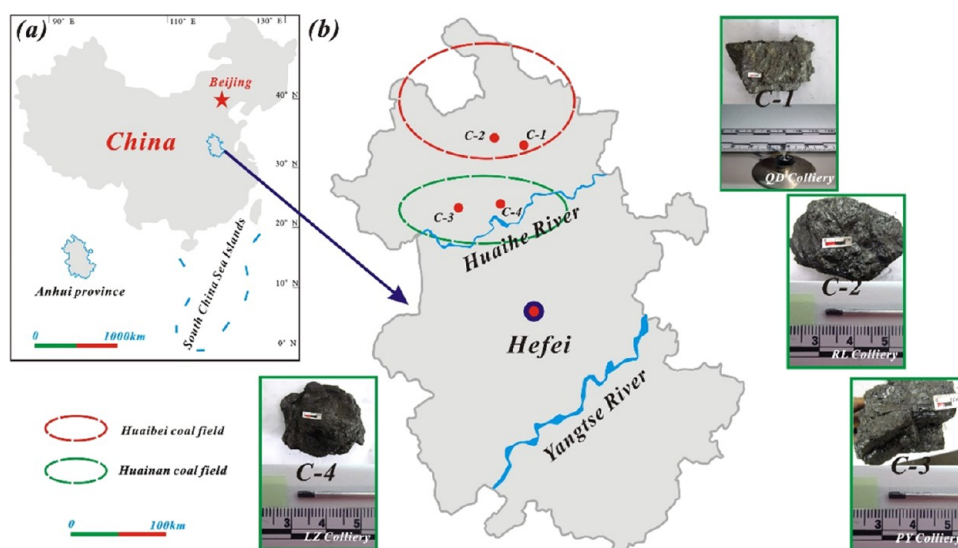
Figure 1. Distribution of coal samples: (a) Chinese map; (b) Anhui province; (c-1) QD sample; (c-2) RL sample; (c-3) PY sample; and (c-4) LZ sample.

Table 1. Key Properties of the Coal Samples Used in This Study[a]

sampling location	$R_{o,max}$/%	proximate analysis/wt %				maceral concentrates/wt %		
		M_{ad}	A_{ad}	V_{daf}	FC_{ad}	V_{it}	I_{ne}	M_{in}
QD	0.88	1.41	16.03	35.29	47.27	59.82	24.38	15.81
RL	0.90	1.46	23.5	28.26	46.78	64.1	21.5	14.4
PY	0.89	1.46	13.5	18.36	66.68	55.53	27.25	17.22
LZ	0.87	1.83	14.44	33.38	50.35	56.315	23.175	20.51

[a]Notes: wt %, weight percent; $R_{o,max/\%}$, average maximum vitrinite reflectance; M_{ad}, moisture; A_{ad}, ash yield; V_{daf}, volatile matter; FC_{ad}, fixed carbon content; V_{it}, vitrinite content; I_{ne}, inertinite content; M_{in}, mineral content; "ad", air-drying base; "daf", dry ash-free basis.

resonance.[9,10] Direct methods include scanning electron microscopy, field emission scanning electron microscopy, and X-ray computed tomography (i.e., CT).[11,12] The comparative analysis of various test methods shows that X-ray CT is a nondestructive three-dimensional (3D) imaging technology, which can use high-resolution images to visualize topological samples and their spatial distribution of pore and fracture structures.[13,14]

The permeability of a coal reservoir is mainly affected by the pore and fracture structures, and its complexity determines the anisotropy of permeability.[15,16] As for the application of X-ray CT technology in the characterization of coal, previous studies mainly focused on the characterization methods of pore and fissure[17] and then proposed complete workflows from pore-scale imaging to determining absolute permeability[18] and studied the impact of image processing methods on the morphology of porous media, pore and fracture structures, and physical properties.[13] Based on the X-ray CT data, there are few studies on the complexity of pore and fracture structures and the heterogeneity of permeability in the direction of coal reservoirs. There are few reports on the relationship among the complexity of pore and fracture structures, the typicality of a fluid migration path, and the heterogeneity of permeability in coal reservoirs.

In this study, crushed soft coal with low permeability from Huainan and Huaibei coalfields of China was taken as the research object. First, a 3D visualization reconstruction of pore and fracture structures was realized. Second, an equivalent pore and fracture network model was constructed. Finally,

permeability evolution and its anisotropy of the coal reservoir were dynamically demonstrated. In this study, the implication of surface porosity on the heterogeneity of pore and fracture structures was first discussed, then the implication of coordination number on the anisotropy of fluid flow was discussed, and finally, the influence of the anisotropy of fluid flow on the CO_2-ECBM process was discussed.

The innovation of the research is mainly reflected in the following aspects: (1) the equivalent pore and fracture network model of crushed soft coal with low permeability is constructed; (2) the evolution and its anisotropy of reservoir permeability are dynamically indicated; (3) the implication of surface porosity on the heterogeneity of pore and fracture structures is discussed; (4) the indication connotation of coordination number on the anisotropy of fluid flow is discussed; and (5) the influence of the anisotropy of fluid flow on the CO_2-ECBM process was analyzed. This study has important theoretical and practical significance for industrial tests and commercialization of CO_2-ECBM technology in crushed soft coal with low permeability.

2. SAMPLES AND METHODS

2.1. Sample Collection and Basic Test. The samples collected in this research are located in the Qidong and Renlou collieries in the Huaibei coalfield and the Panyi and Liuzhuang collieries in the Huainan coalfield, and the sample numbers are QD, RL, PY, and LZ, respectively (Figure 1). Samples were collected from fresh working surfaces, and they were collected, packed, and transported in accordance with relevant national
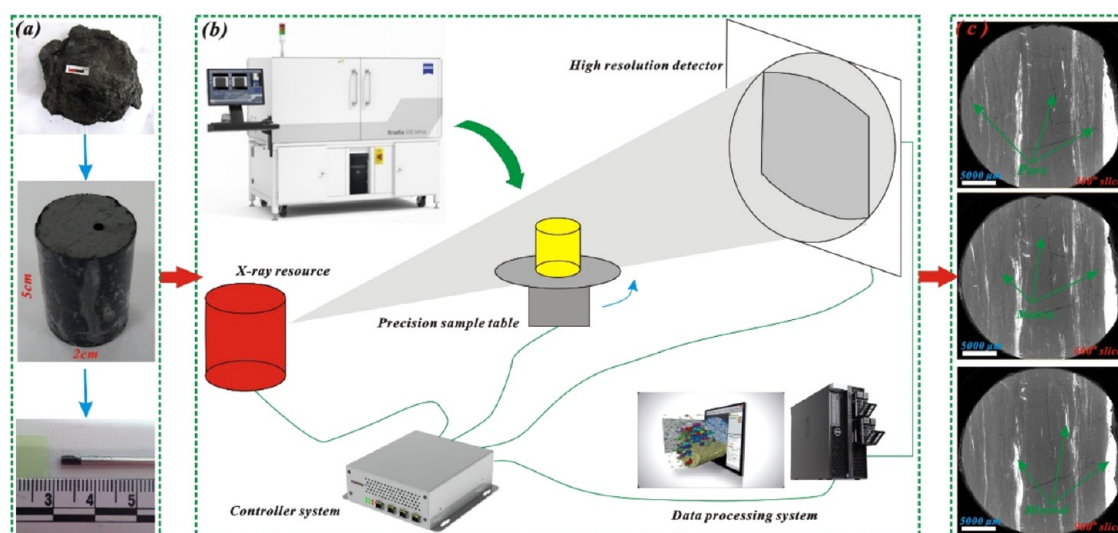
Figure 2. X-ray CT scanning system. (a) Preparation of sample; (b) imaging system components; (c) typical 2D CT slices of a coal sample.

and international standards with GB/T 6948−2008 and GB/T 8899−2013.[19,20]

According to the results of the vitrinite reflectance test and the coal industry standard with MT/T1053−2008, coal samples from QD, RL, PY, and LZ collieries are bituminous coal, and other results of the basic test analysis are shown in Table 1.

2.2. Sample Preparation and Scanning. In this study, X-ray CT scanning adopts the Xradia 520 Versa CT scanning system produced by Carl Zeiss of Germany, which mainly includes core components such as X-ray source, precision sample table, high-resolution detector, data processing system, and controller system (Figure 2). The maximum power of the X-ray light source is 10 W, the maximum voltage is 140 kV, and its scanning resolution is between 0.7 and 50 μm (Figure 2). When the sample is rotated on the sample table, the X-ray tube emits X-rays. X-rays pass through the sample and are attenuated by the photoelectric effect. A flat panel detector collects the attenuated X-ray beam and measures its cumulative attenuation. The signal conversion system receives the input signal from the flat panel detector and uses the image reconstruction algorithm to generate the grayscale image of the slice sequence (Figure 2).

Fresh block samples were prepared into column samples with a height of no more than 5 cm and a diameter of no more than 2 cm for the testing company to complete further sample preparation and scanning work (Figures 1 and 2a). The resolution between the samples ranged from 3.59 to 10.00 μm. After an X-ray CT scan, nearly 2000 slices with the size of nearly 1800 × 1800 voxels can be obtained from four samples (Table 2). After scanning, the black, gray, and white areas in the typical slices represent pore and fracture, matrix, and mineral phases, respectively (Figure 2c).

2.3. Reconstruction Processing for Sample Visualization. The 3D visual reconstruction of coal can be completed based on the typical slices obtained by scanning, the core steps of which include the selection of representative element volume (i.e., REV), the noise reduction processing of the image, and threshold selection and image segmentation (Figure 3). The size of the REV can be determined by analyzing the variation law of porosity and the size of REV.[21,22] The median filter process can well protect the integrity of the

Table 2. Dimensions of the Four Coal Samples Used in This Study

sample ID	sample shape	number of voxels	voxel size (μm)
QD	cylindrical type	1060 × 1019 × 2429	3.59
RL	cylindrical type	1810 × 1801 × 2001	8.02
PY	cylindrical type	1763 × 1784 × 1972	8.45
LZ	cylindrical type	2500 × 2500 × 1900	10.00

pore and smooth the transition between the pore and the matrix, so that the pore and fracture can be well distinguished from other components.[23,24] The watershed algorithm can be used to select thresholds for the pore and fracture, matrix, and mineral phases (Figure 3).[25,26] Based on the above core steps, the 3D visualization reconstruction of the pore and fracture structures can be realized.

After the pore and fracture space of the coal reservoir is obtained, the equivalent pore and fracture network model can be established by using a morphological algorithm, namely, the central axis algorithm,[27,28] which can simplify the characterization of pore and fracture structures. In the model, the pore space is divided into two parts with a pore and a throat, wherein the central axis nodes of the pore space are defined as pores and the connecting lines between nodes are defined as throat (Figure 4).[29] As shown in Figure 4b, the sphere represents the pore and the tube bundle represents the throat.

2.4. Model Construction and Boundary Condition Loading of Permeability. Based on the equivalent pore and fracture network model and the analysis of pore and throat parameters, the fluid migration capacity in a coal reservoir can be discussed, and the most important parameter is absolute permeability. Based on the discussion of Poiseuille's law,[30] and the analysis of structural parameters with pore and fracture length, throat radius, and dynamic viscosity coefficient, the fluid conductivity can be calculated, which can be characterized as follows[30]

$$g_{ij} = \frac{\pi}{8\mu} \frac{r_{ij}^4}{l_{ij}} \tag{1}$$

where g_{ij} is the conductivity coefficient, l_{ij} is the length of the pore and throat, r_{ij} is the radius of the pore and throat, and μ is
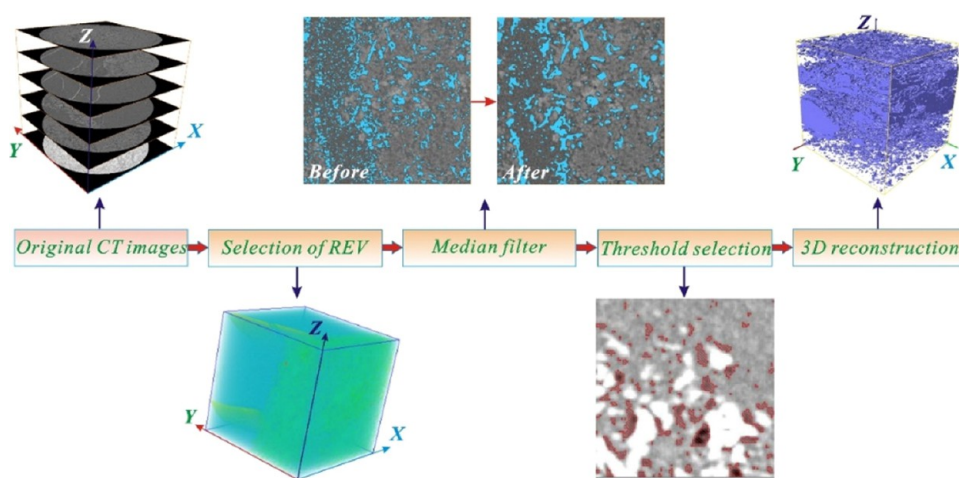
Figure 3. Schematic diagram of the reconstruction processing for sample visualization.
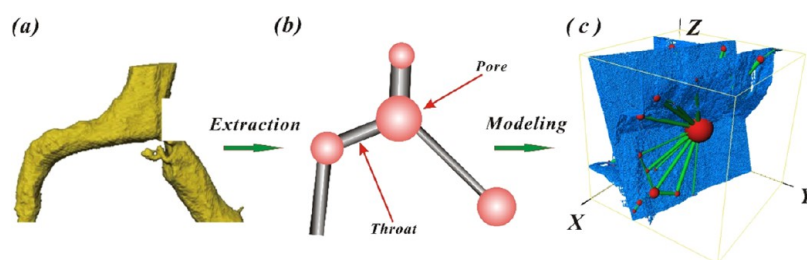

Figure 4. Equivalent pore and fracture network model constructed by the central axis algorithm. (a) Real pore and fracture; (b) pore and fracture diagram based on the central axis algorithm; and (c) superposition of the interconnected pore and fracture and the equivalent pore and fracture network model.
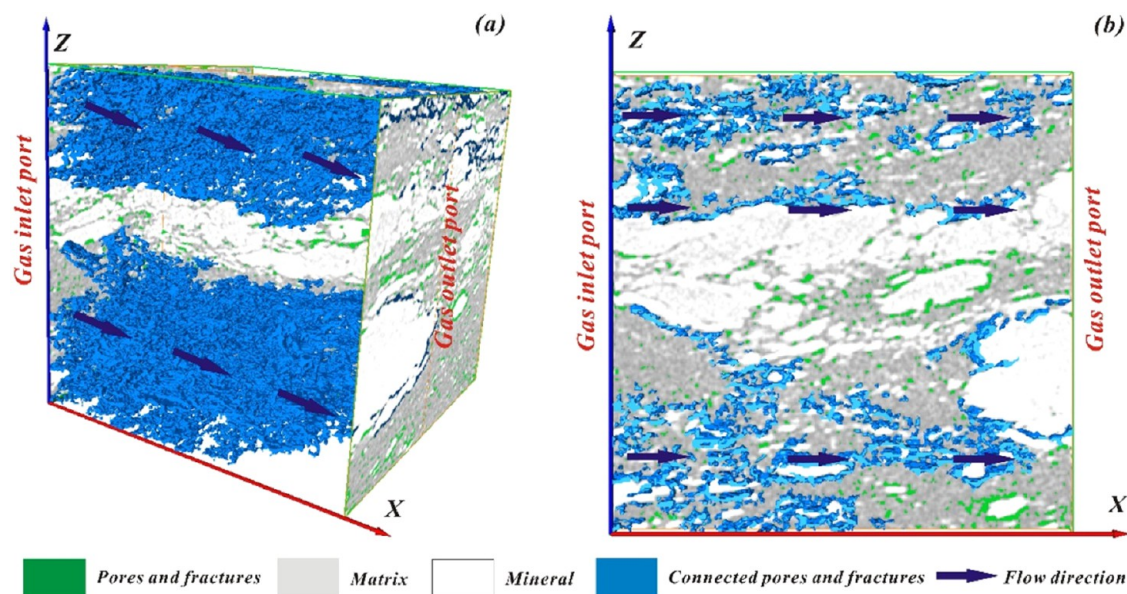

Figure 5. Loading of boundary conditions for the fluid permeability test in an equivalent pore and fracture network model. (a) Three-dimensional perspective, and (b) two-dimensional perspective.

the dynamic viscosity. There is a pressure difference in the flow of the fluid in pore and fracture network model, and the fluid velocity in the pore has a linear relationship with the pressure drop, which can be characterized as follows[30]

$$q_{ij} = g_{ij}(P_i - P_j) \qquad (2)$$

where q_{ij} is the fluid flow, P_i is the pressure at point i in the pore and throat, and P_j is the pressure at point j in the pore and throat. Based on the analysis of the mass conservation law at each node in the pore and fracture system, the fluid continuity equation can be obtained, which can be characterized as follows

$$\sum_{i \to j} q_{ij} = 0 \qquad (3)$$

The total flow Q in the pore and throat of the pore and fracture network model is obtained by adding the flow q_{ij} in each pore and throat, and its permeability is positively correlated with the total flow, which can be characterized as follows[24]

$$k = \frac{Q}{\Delta P} \frac{\mu L}{A} \qquad (4)$$

where k is equivalent permeability in pores and fractures, L is the throat length of fluid flow, and A is the cross-section area of the flow channel. In this study, the fluid was set as CO_2, its dynamic viscosity was 1.38×10^{-4} Pa·s, and inlet and outlet pressures were 0.13 and 0.10 MPa, respectively. The loading of specific boundary conditions is shown in Figure 5.

3. RESULTS

Based on the original CT slices obtained by X-ray CT scanning, the 3D visualization reconstruction of the pore and fracture structures can be realized. Based on the central axis algorithm, the equivalent pore and fracture network model can be constructed, the pore and throat can be extracted further, and then the geometric and topological structures of the pore and fracture can be analyzed. Based on the established equivalent pore and fracture network model, dynamic representation and anisotropy analysis of the absolute permeability of the coal reservoir can be realized.

3.1. 3D Visualization Reconstruction of Pore and Fracture Structures.

The basic idea of the watershed segmentation algorithm is as follows: the whole image is regarded as a rugged mountain model, the gray value of each pixel represents the elevation of the point, and the local minimum area in the image corresponds to the catchment basin in the landform (Figure 6). The A, B, C, and D areas are
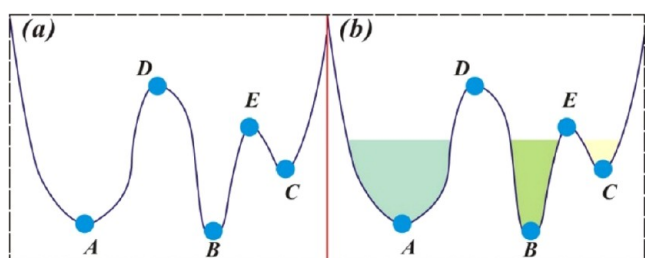

Figure 6. Schematic diagram of the Watershed algorithm. (a) Terrain section of the Watershed algorithm. (b) Flooding diagram of the Watershed algorithm. A, B, and C are the basin floor, and D and E are the ridge of mountains.

the minimum points, that is, the pelvic floor, and the E, F, and G areas are the ridges. During the simulated water injection process, the water surface slowly spreads from the bottom of the mountain to the top of the mountain, and as the water level rises, the catchment basin will be flooded and merged into the same area. In order to prevent consolidation, "dikes" can be built between catchment basins to form watersheds (Figure 6).[25,26]

By analyzing the variation law of the porosity between the four scanned samples and the size of the REV, it can be seen that $400 \times 400 \times 400$ voxels is more appropriate for the size of the REV (Figure 7), which can take into account the

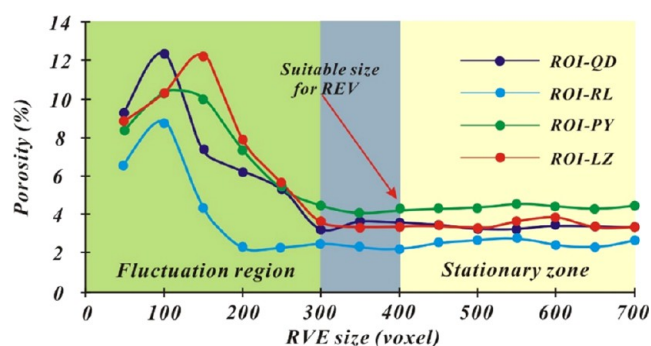complexity and heterogeneity of the sample, and the memory capacity of the computer.

Figure 7. Changes in the porosity of the test sample and its REV size.

Based on the watershed algorithm, the pore and fracture structures of the coal reservoir can be extracted and visually reconstructed in the RVE domain with $400 \times 400 \times 400$ voxels (Figure 8).

The results of visual reconstruction among samples all show that the coal reservoir structure has a high spatial heterogeneity. The silver area characterizes mineral, which mainly distributes in the middle space of the coal sample with an irregular shape. The gray area represents the matrix, which occupies the largest proportion in coal. The red area represents pore and fracture, which are ellipsoidal and conical in various regions of the sample space (Figure 8). Among the samples, the proportion of pore and fracture phases is between 2.17 and 4.23%, the proportion of the matrix phase is between 91.13 and 95.19%, and the proportion of the mineral phase is between 1.59 and 4.34%. The data of the pore and fracture, matrix, and mineral phases also explain the heterogeneity of the coal reservoir structure.

3.2. Reconstruction and Parameter Analysis of the Interconnected Pore Structure.

The connectivity of pore space is an important topological information on porous media, which affects the overall physical properties of porous media. In a certain direction of the 3D digital coal, if the pore phase is continuous from one end to the other, it means that the digital coal is connected in that direction. Digital coal is composed of a large number of discrete pixels, and the connectivity between pixels can be described in three ways: 6-connected, 18-connected, and 26-connected (Figure 9).[31,32] In this study, 6-connection processing was used to analyze connectivity, that is, voxels with common faces are considered to be connected.

By using the 6-connection method for connectivity analysis, the equivalent interconnected pores and fractures can be further extracted within the extracted equivalent pores and fractures (Figure 10).

For the QD sample, the development scale of the interconnected pores and fractures is relatively uniform in the three directions. For the RL sample, the development scale of the interconnected pores and fractures in the Y and Z directions is obviously stronger than that in the X direction. For the PY sample, the development scale of the interconnected pores and fractures in the X and Y directions is obviously stronger than that in the Z direction. For the LZ sample, the development scale of the interconnected pores and fractures in the three directions is relatively uniform, and the
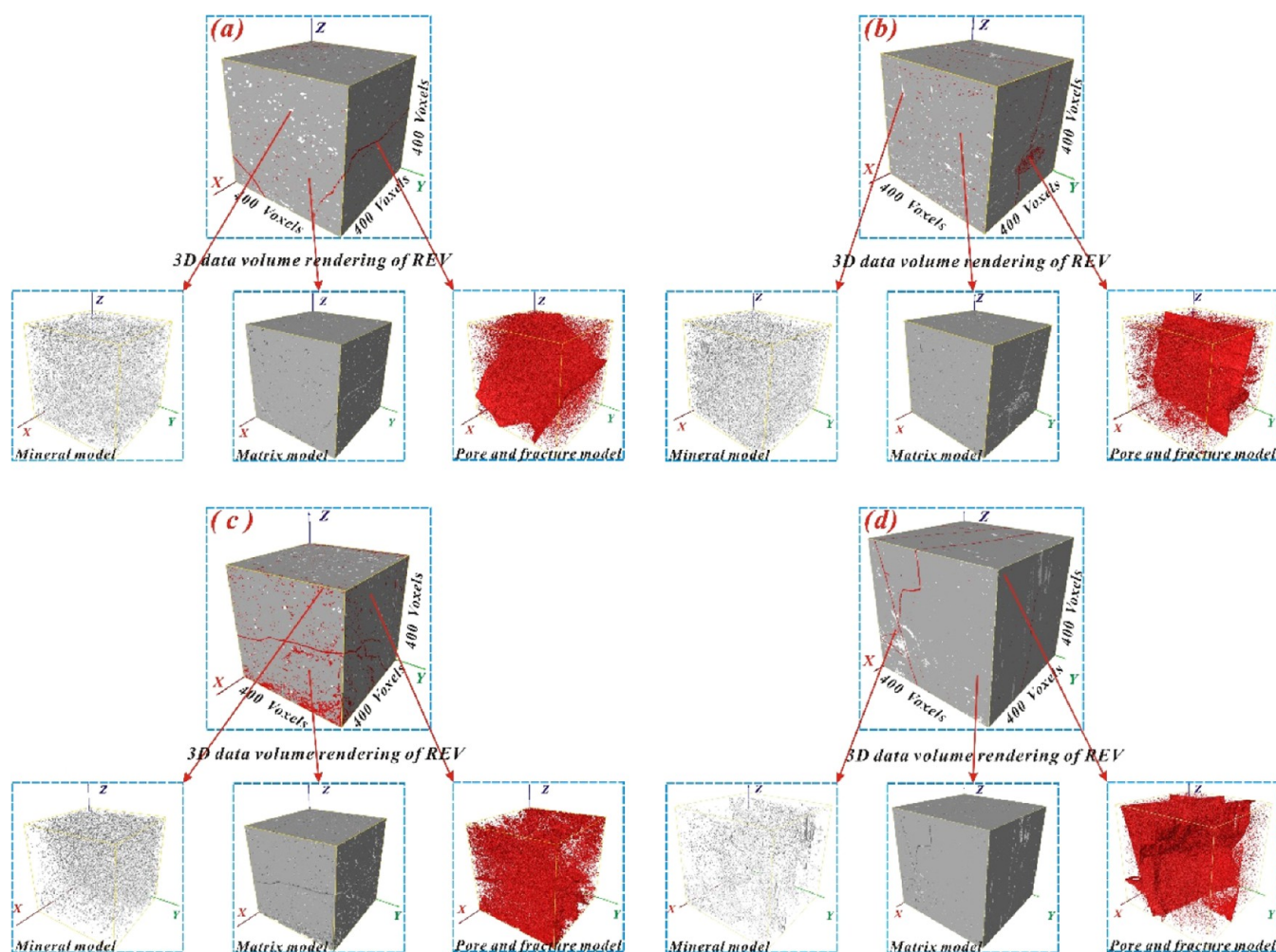
Figure 8. Structure data extraction and 3D visualization reconstruction of the coal reservoir. (a) QD sample; (b) RL sample; (c) PY sample; and (d) LZ sample.
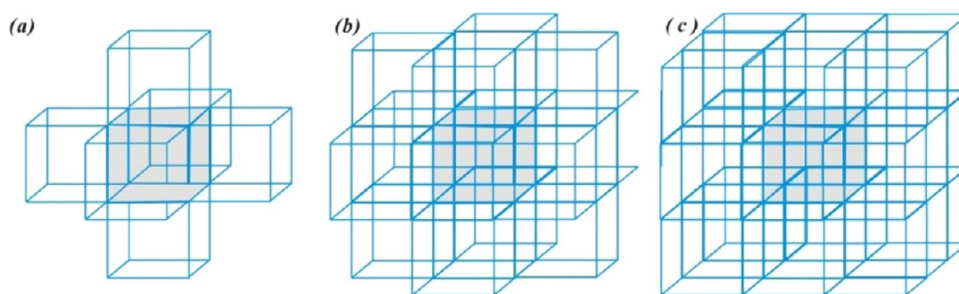

Figure 9. Schematic diagram of extraction of minerals touched by interconnected pores and fractures: (a) 6-connectivity; (b) 18-connectivity; and (c) 26-connectivity.

scale in each direction is stronger than that in the other samples (Figure 10). The differences in the development of the interconnected pores and fractures in different directions indicate the complexity of pore and fracture structures in coal reservoirs, which in turn indicates the heterogeneity of permeability.

Based on the data of the pore and fracture phases and their interconnected pore and fracture phases, structural parameters such as porosity, interconnected porosity, and the connectivity coefficient can be analyzed, and the relevant calculation formulas can be characterized as follows

$$\varphi_{\text{coal}} = \frac{V_{\text{pore}}}{V_{\text{coal}}} \tag{5}$$

$$\varphi_{\text{interconnected-pore}} = \frac{V_{\text{interconnected-pore}}}{V_{\text{coal}}} \tag{6}$$

$$\eta = \frac{\varphi_{\text{interconnected-pore}}}{\varphi_{\text{coal}}} \tag{7}$$

where φ_{coal} is the digital coal porosity in REV, V_{pore} is the pore volume, V_{coal} is the digital coal volume in REV, $\varphi_{\text{interconnected-pore}}$ is the interconnected porosity, $V_{\text{interconnected-pore}}$
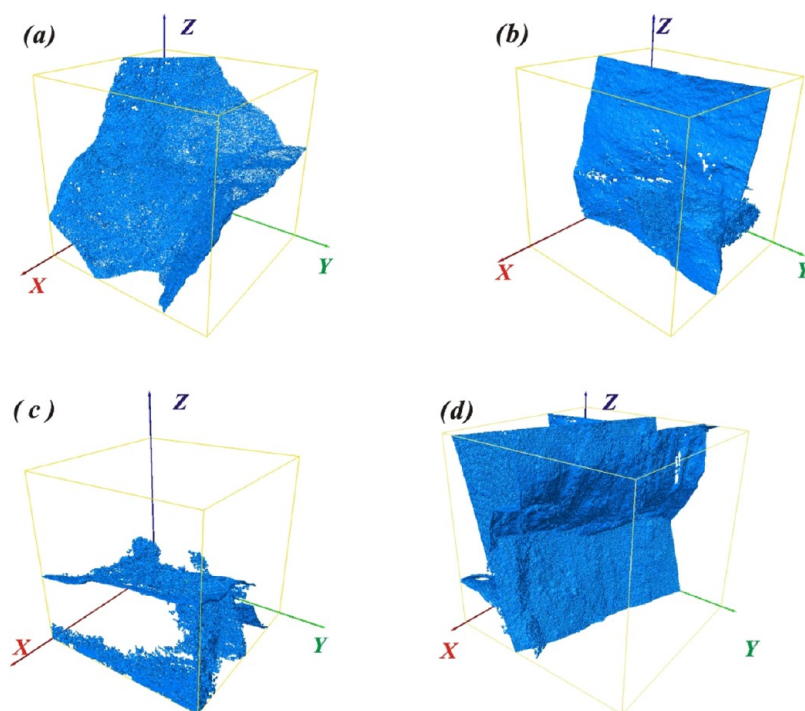
Figure 10. Extraction and reconstruction of interconnected pores and fractures of test samples: (a) QD sample; (b) RL sample; (c) PY sample; and (d) LZ sample.

is the connected pore volume, and η is the connectivity coefficient. The parameters of interconnected pores and fracture in the coal are shown in Table 3.

Table 3. Analysis of the Connectivity Parameters for the Interconnected Pore and Fracture

sample ID	porosity	interconnected porosity	isolated porosity	connectivity (%)
QD	3.37	1.07	2.3	31.75
RL	2.17	1.57	0.6	72.35
PY	4.23	1.53	2.7	36.17
LZ	3.55	2.56	0.99	72.11

It can be seen from Table 3 that the sample porosity is between 2.17 and 4.23, and the PY sample is the best. The connectivity porosity is between 1.07 and 2.56, especially that of the LZ sample. The connectivity coefficient was between 31.75 and 72.35%, especially for the RL sample. According to the parameters used to characterize the connectivity of pore and fracture structures, the LZ sample has the best connectivity, the most developed pore and fracture system, and the strongest fluid migration ability.

3.3. Model Extraction and Parameter Analysis of the Equivalent Pore and Fracture Networks. Based on the central axis algorithm, the equivalent pore and fracture network model of the scanned sample can be constructed (Figure 11), and the data extraction and analysis of structural parameters such as equivalent pore diameter, equivalent throat diameter, pore volume, throat surface area, and coordination number can be realized.

As can be qualitatively seen from Figure 11, the interconnected pore and fracture structures of LZ and RL samples are more developed than those of PY and QD samples, and the connected pore and fracture structures are

more balanced in terms of the number of pores and throats, especially the LZ sample is the most developed and more balanced. The interconnected pore and fracture structures of the QD sample are relatively poor in quantity and balance. The LZ sample is connected in all three directions, and the connectivity advantage is much greater than the other samples. Based on the equivalent pore and fracture network model constructed, the core parameters of their geometric and topological structures can be analyzed (Table 4).

It can be seen from Table 4 that in the equivalent pore and fracture network model, the pore and throat numbers of RL, PY, and LZ samples are much larger than that of the QD sample, and the ratio of pore and throat numbers of RL and LZ samples is much larger than that of QD and PY samples. The average values of the pore radius, throat radius, and length of the LZ sample are 44.24, 26.27, and 147.36 μm, respectively, and the pore and throat also have obvious advantages in the scale of pore space (Table 4).

In terms of coordination number, the QD, RL, PY, and LZ are between 1 and 18, 1−47, 1−33, and 1−40, respectively, with average values of 4.76, 5.99, 4.87, and 5.78 (Table 4). The coordination number of LZ and RL samples is much larger than that of QD and PY samples, which indicates that there are more throats connected with pores, and the connectivity is better, and the migration ability of the fluid is stronger. The distribution range of the coordination number is wide, and when it is greater than 15, the number is scattered. Therefore, the distribution analysis of the coordination number between 1 and 15 of the testing samples is emphasized (Figure 12).

The coordination number of the testing samples is relatively large in the range of 2−8, and the value 5 is the optimal proportion, accounting for 18%, which indicates that about 18% of the pores are mainly connected by five throats in the connected pores and fractures, especially in RL and LZ samples (Figure 12), which is consistent with the connectivity
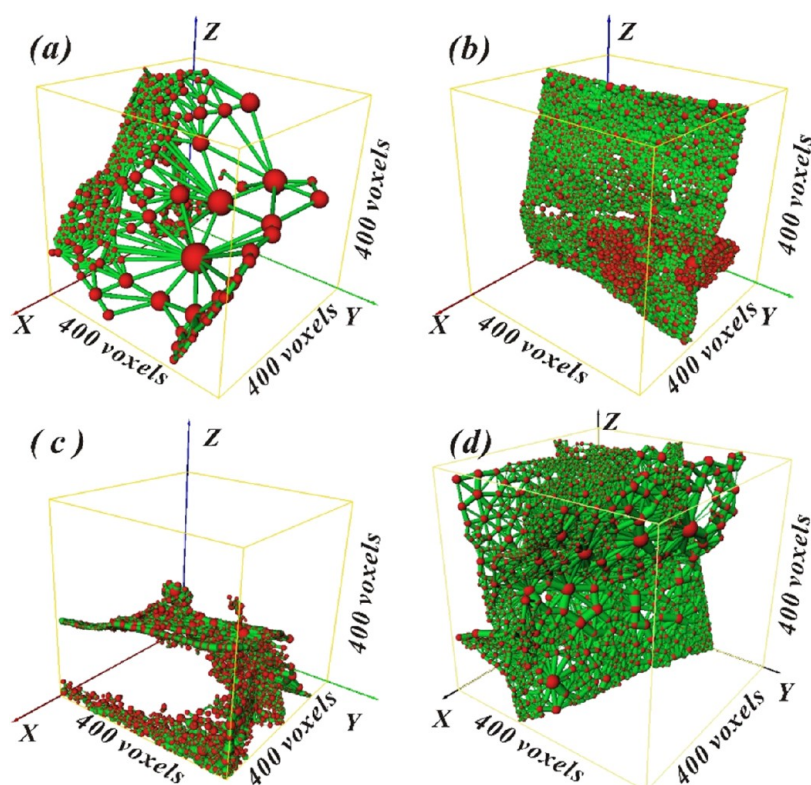
Figure 11. Equivalent network model of the interconnected pore and fracture: (a) QD sample; (b) RL sample; (c) PY sample; and (d) LZ sample.

Table 4. Analysis of Core Parameters of the Geometric and Topological Structure of the Equivalent Network Model with Interconnected Pores and Fractures

sample ID	value	pore radius (μm)	throat radius (μm)	throat length (μm)	coordination number	pore number	throat number	ratio of pore and throat
QD	max.	88.73	25.46	640.88	18	381	905	2.38
	min.	2.81	0.95	6.39	1			
	ave.	21.84	8.23	94.94	4.76			
RL	max.	73.52	39.14	278.88	47	3816	11431	3.00
	min.	3.99	1.56	11.91	1			
	ave.	23.40	11.10	66.29	5.99			
PY	max.	79.04	51.72	481.92	33	2749	6692	2.43
	min.	8.05	1.73	8.10	1			
	ave.	28.63	13.50	86.38	4.87			
LZ	max.	195.93	119.95	1117.49	40	2471	7127	2.88
	min.	6.20	2.66	16.96	1			
	ave.	44.24	26.27	147.36	5.78			

analysis data of 3D pore and fracture and the construction results of the equivalent network model of interconnected pores and fractures (Table 3 and Figure 11).

3.4. Dynamic Diagram and Anisotropic Analysis of Permeability. Based on the equivalent pore and fracture network model extracted, the flow state of a fluid in its interior can be simulated, and its migration path can be visualized (Figure 13). The size of the sphere corresponds to the volume of the equivalent pore and fracture. The color of the sphere represents the pressure of this point. In this study, the color of the sphere changes from blue to red, which indicates that the pressure gradually increases. The radius of the throat represents the corresponding fluid flow, and the larger the radius is, the larger is the flow (Figure 13).

It can be seen from Figure 13 that not all pores and fractures have fluid flow in the equivalent network model. There is no

significant flow flux between most pores, and only a small number of flow paths exist in the overall pore structure. The flow rate in throats connected by small pores is small, and the fluid flow between large pore sizes is more significant. On the whole, the development advantages of the flow path of RL and LZ samples are obvious (Figure 13), which indicates that the pore and fracture structures of RL and LZ samples are conducive to better fluid migration. The fluid migration capacity of a pore fracture structure of a coal reservoir can be quantitatively characterized by permeability. Based on the equivalent pore and fracture network model extracted, permeability changes in different directions of the reservoir can be simulated (Table 5) so as to characterize the pore and fracture structures of the coal reservoir and the heterogeneity of its corresponding permeability.
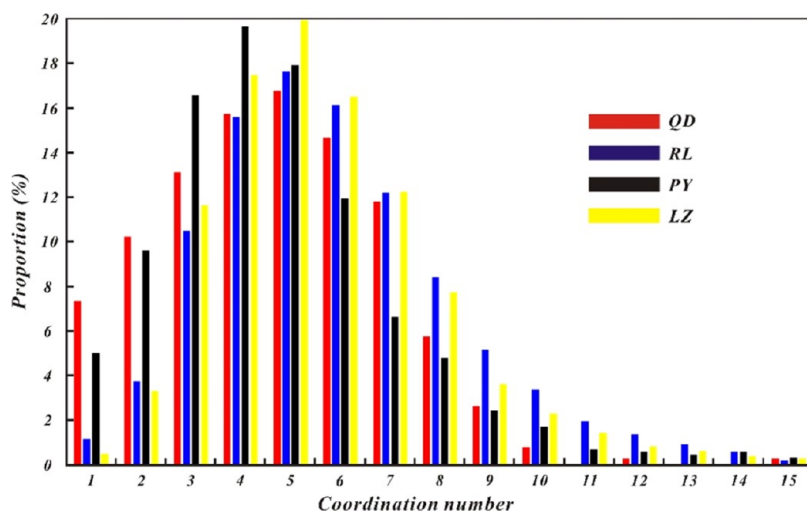
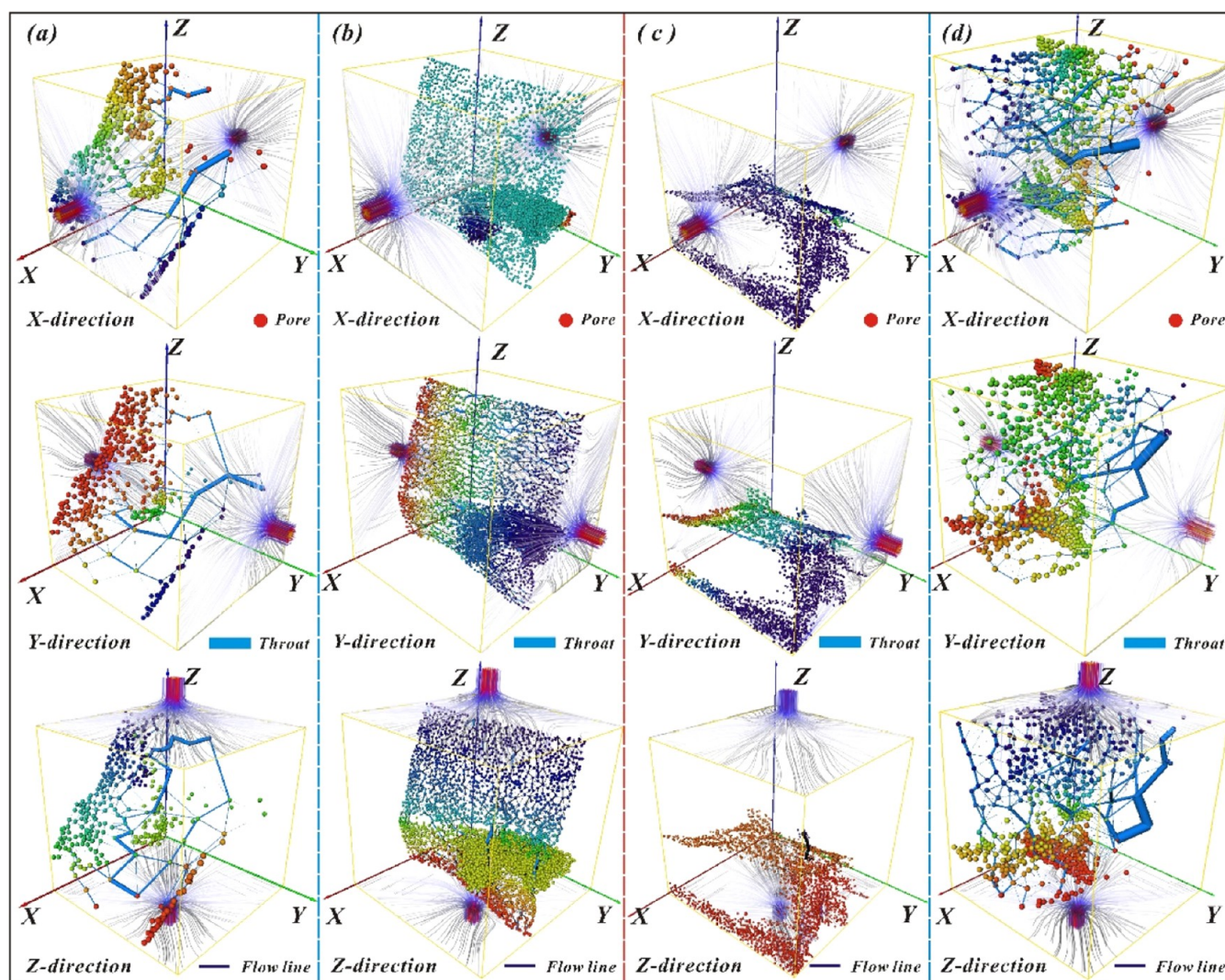**Figure 12.** Distribution of the coordination number for four samples.

Figure 13. PNM-based visualization of 3D directional gas migration paths: (a) QD sample; (b) RL sample; (c) PY sample; and (d) LZ sample.

By analyzing the data in Table 5, it can be seen that the absolute permeability of the QD sample is significantly lower than that of the other three samples, which is in good agreement with the analysis results of the fluid migration path in the pore and fracture structures in Figure 13. The absolute permeability of each sample varies greatly in different directions, which indicates the heterogeneity of pore and fracture structures of the coal reservoir. For the QD sample,

Table 5. Calculated Permeability Values in Three Dimensions (mD)

direction	QD	RL	PY	LZ
X	757.5	1939.33	4022.34	5481.92
Y	647.6	3838.59	3293.71	5037.85
Z	747.2	3892.05	1684.73	4846.08
ave.	717.43	3223.32	3000.26	5121.95

the absolute permeability in different directions is little different, and the absolute permeability in the Y direction is relatively low, which is in good agreement with the analysis results of the migration path of the equivalent pore and fracture network model. For the RL sample, the migration path analysis of the equivalent pore and fracture network model shows that the migration path in the X direction is weaker than that in the Y and Z directions, which indicates that the connectivity of the RL sample in this direction is relatively poor, and it is in good agreement with the simulation results of absolute permeability. For the PY sample, the absolute permeability in the X and Y directions is better than that in the Z direction. For the LZ sample, the absolute permeability is large in all directions, which indicates that the sample permeability is good. The numerical differences of permeability between samples and in all directions are in good agreement with the migration path analysis results of the equivalent pore and fracture network model (Figure 13 and Table 5).

4. DISCUSSIONS

4.1. Implication of Surface Porosity on the Characterization of Heterogeneity of Pore and Fracture Structures. In 3D space, the connectivity porosity and

coefficient can provide a preliminary understanding of the fluid migration capacity in the pore and fracture structures. In the two-dimensional (2D) plane, surface porosity, that is, the ratio of pore area in the 2D slice image to the slice area, can be used to further analyze the complexity of pore and fracture structures and characterize the heterogeneity of pore and fracture structures in a coal reservoir. When the surface porosity is 0 or close to 0, this indicates that the pore structure is not interconnected or has poor connectivity. The surface porosity of the four samples with different directions can be shown in Figure 14.

For the QD sample, the surface porosity significantly changes in the Y and Z directions, which indicates that the heterogeneity in the Y and Z directions is significantly higher than that in the X direction. The surface porosity in the Y direction is relatively small, which indicates that the sample connectivity in this direction is relatively poor. For the RL sample, the surface porosity significantly changes in the X and Z directions, which indicates that the heterogeneity in the X and Z directions is significantly higher than that in the Y direction. The surface porosity in the X direction is relatively small and nearly 0, which indicates that the sample connectivity in this direction is relatively poor. For the PY sample, the surface porosity changes significantly in the Z direction, which indicates that the heterogeneity in the Z direction is significantly higher than that in the X and Y directions. For the LZ sample, the surface porosity changes significantly in the X and Y directions, which indicates that the heterogeneity in the X and Y directions is significantly higher than that in the Z direction (Figure 14). The average surface porosity values of QD, RL, PY, and LZ samples are in the ranges of 0.10−0.25, 0.20−0.30, 0.30−0.40, and 0.30−0.50,
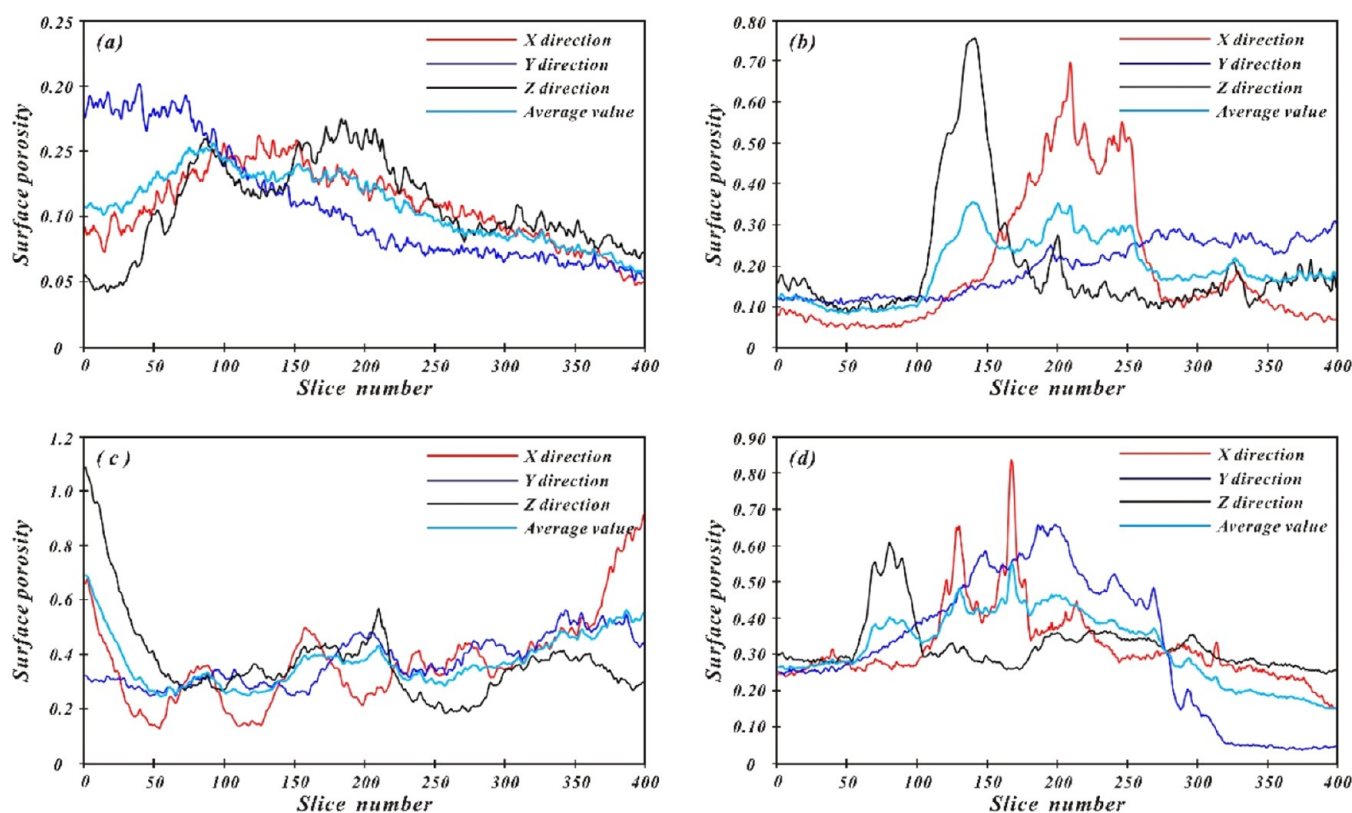

Figure 14. Surface porosity distribution for the 2D pore structures. (a) QD sample, (b) RL sample, (c) PY sample, and (d) LZ sample.
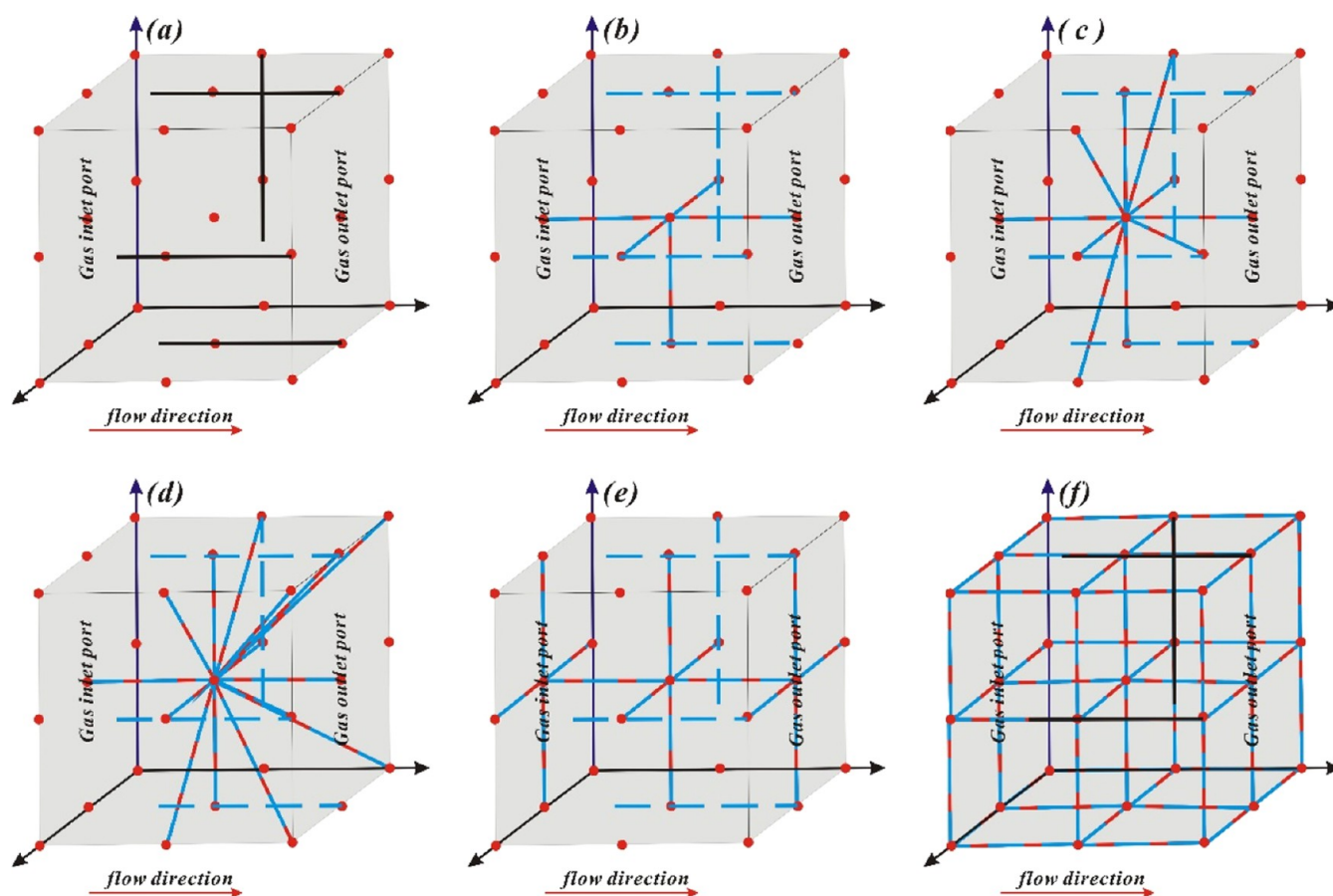
Figure 15. Influence of coordination number on the connectivity of pores and fractures. The coordination number gradually increases from (a) to (f).
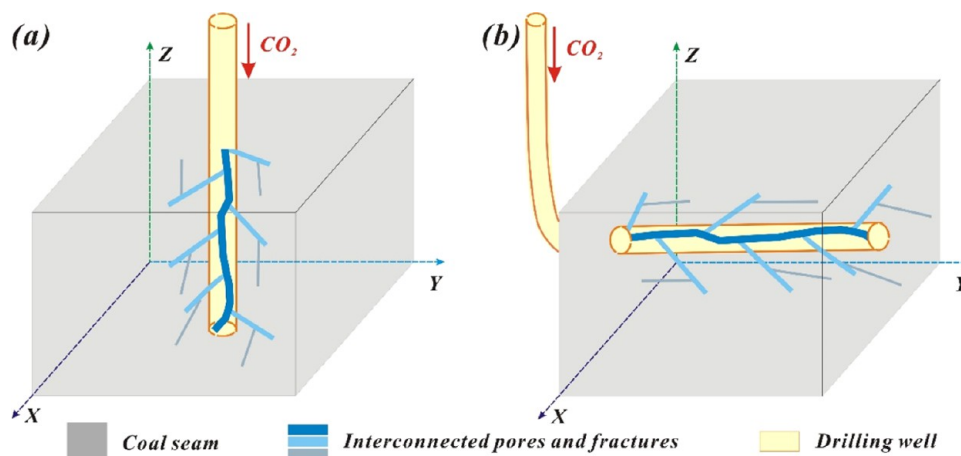

Figure 16. Schematic diagram of the relationship between directional differences in the development of connected pores and fractures and drilling design. (a) Pores and fractures are mainly vertically developed, and (b) pores and fractures are mainly horizontally developed.

respectively, and the surface porosity of the LZ sample is the best, which is in good agreement with the analysis results of porosity, connectivity porosity, and connectivity coefficient on the 3D scale of pore and fracture structures (Figure 14). The analysis results of surface porosity are also in good agreement with the difference of permeability in different directions and the analysis results of the migration path of the equivalent pore and fracture network model (Figures 13 and 14; and Table 5).

4.2. Implication of Coordination Number on the Anisotropy of Fluid Flow. The 3D pore and fracture network model can be characterized as dual media models, which includes the basic units of pores, throats, and microfractures and represents the pores, throats, and microfractures during fluid migration, respectively (Figure 15). The red sphere represents the pores, the black column represents the microfractures, the blue dashed line represents the fluid migration area, the red column represents the throats, and the direction of the red arrow represents the fluid migration direction (Figure 15).

Taking the pore in the central region in Figure 15a−c as the object, the influence of coordination number on the connectivity of the pore and fracture can be quantified. In Figure 15a−c, the coordination numbers are 0, 5, and 10, respectively. With the gradual increase of coordination number, the number of throats connected with pores also gradually increases, and the connectivity of the sample gradually improves with the expansion of the connected region (Figure 15a−c), which well explains why the permeability of the LZ and RL samples is stronger than that of the QD and PY samples.

Taking the pore and throat in Figure 15d−f as an object, the influence of the balance of their number on the connectivity of pore and fracture can be quantified. By comparing the quantitative balance difference between pores and throats in Figure 15d−f, it can be seen that when the quantitative balance between pores and throats is poor, the active area of a fluid is often limited to one end of the model, which will then affect the connectivity of pores and fractures (Figure 15d). When the number of pores and throats is well-balanced, that is, the number of throats is roughly equal to the number of pores and fractures, and the active areas of the fluid are spread throughout the model, the connectivity of the pores and fractures of the sample is good (Figure 15f), which also explains why the permeability of the LZ sample is stronger than that of the other samples.

4.3. Influence of the Anisotropy of Fluid Flow on Drilling Design during the CO₂-ECBM Process. The CO₂-ECBM process is a competitive adsorption process of CO_2 and CH_4 in coal reservoirs. How to improve the CO_2 injection and CH_4 production efficiencies is the core issue that needs to be considered in the promotion of CO₂-ECBM technology, which is closely related to the development of pores and fractures in a coal reservoir. From the macroscale to microscale, the differences in the direction of the development of pores and fractures in a coal reservoir will affect the drilling design of CO₂-ECBM technology, as shown in Figure 16.

When the primary interconnected pores and fractures in a reservoir mainly develop vertically and the secondary and tertiary interconnected pores and fractures develop successively, with extend along the Z axis and expand along the X and Y axis, the drilling construction of CO₂-ECBM technology should focus on the vertical well design, and the well location in this direction can connect the vertical connected pores and fractures to the greatest extent. Thus, the injected CO_2 can be in contact with the coal reservoir to a greater extent, and the adsorption capacity of the coal reservoir for CO_2 is greater than that of CH_4, so that geological storage of CO_2 and production increase of CH_4 can be realized (Figure 16a). When the primary interconnected pores and fractures in a coal reservoir mainly develop horizontally, and the secondary and tertiary interconnected pores and fractures develop successively, which extend along the X and Y axes and expand along the Z axis in general, the drilling construction of CO₂-ECBM technology should focus on the horizontal well design, so as to improve the injection and production efficiencies of CO₂-ECBM technology (Figure 16b).

5. CONCLUSIONS

In this study, crushed soft coal with low permeability from Huainan and Huaibei coalfields of China was taken as the research object. First, the 3D visualization reconstruction of pore and fracture structures was realized. Second, the

equivalent pore and fracture network model was constructed. Finally, the permeability evolution and its anisotropy of a coal reservoir were dynamically demonstrated. In this study, the implication of surface porosity on the heterogeneity of pore and fracture structures was first discussed, then the implication of coordination number on the anisotropy of fluid flow was discussed, and finally, the influence of the anisotropy of fluid flow on the CO₂-ECBM process was discussed. The main conclusions are as follows.

(1) The visualization characterization and reconstruction of a reservoir structure can be realized based on the analysis of REV, the denoising processing of an image, and threshold selection and image segmentation. Based on the 6-connection method and the central axis algorithm, the equivalent pore and fracture network model of an interconnected pore and fracture in a coal reservoir can be constructed, and parameters such as equivalent pore diameter, equivalent throat diameter, pore volume, and throat surface area can be discussed.

(2) The data analysis results of sample porosity, connectivity porosity, typical path of fluid migration, absolute permeability, and surface porosity have good consistency in characterizing the heterogeneity of pore and fracture structures and permeability of the sample, which is mainly reflected in that the connectivity and permeability of LZ and RL samples are obviously better than those of PY and QD samples. The pore and fracture structures of each sample are different, and the heterogeneity of permeability in different directions is obvious.

(3) The average coordination numbers of QD, RL, PY, and LZ samples are 4.76, 5.99, 4.87, and 5.78, respectively, the number of pores and throats in LZ and RL samples is better, which indicates that more channels and pores are interconnected in LZ and RL samples, the fluid activity area is spread throughout the entire model, and the connectivity of pores and fractures of LZ and RL samples is better. The fluid migration ability is stronger, which is suitable for the industrial test of CO₂-ECBM technology.

(4) When the interconnected pores and fractures mainly develop vertically and extend along the Z axis, the drilling construction of CO₂-ECBM technology should focus on the vertical well design, and the well location in this direction can connect the vertical connected pores and fractures to the greatest extent, so that the geological storage of CO_2 and the production increase of CH_4 can be realized. When the interconnected pores and fractures in a coal reservoir mainly develop horizontally and extend along the X and Y axes, the drilling construction of CO₂-ECBM technology should focus on the horizontal well design.

■ AUTHOR INFORMATION

Corresponding Authors

 Jilin Wang − *Key Laboratory of Coalbed Methane Resources and Reservoir Formation Process, Ministry of Education, China University of Mining and Technology, Xuzhou 221008, China; School of Resources and Geosciences, China University of Mining and Technology, Xuzhou 221116, China;* ◉ orcid.org/0000-0001-5122-5427; Email: wjl_cumt@163.com

Huihuang Fang − *School of Earth and Environment, Anhui University of Science and Technology, Huainan, Anhui 232001, China; Institute of Energy, Hefei Comprehensive National Science Center, Hefei 230000, China;* ● orcid.org/0000-0002-1139-5525; Email: huihuangfang@aust.edu.cn

Authors

Wan Cao − *School of Resources and Geosciences, China University of Mining and Technology, Xuzhou 221116, China*

Bicong Wang − *School of Resources and Geosciences, China University of Mining and Technology, Xuzhou 221116, China*

Xinghe Wu − *School of Resources and Geosciences, China University of Mining and Technology, Xuzhou 221116, China*

Complete contact information is available at:
https://pubs.acs.org/10.1021/acsomega.3c06294

Notes

The authors declare no competing financial interest.

■ REFERENCES

(1) Busch, A.; Gensterblum, Y. CBM and CO_2-ECBM related sorption processes in coal: A review. *Int. J. Coal Geol.* **2011**, 87 (2), 49−71.

(2) Wang, F. F.; Zhang, X. D.; Wu, C. F.; Zhang, S.; Wang, K. Mechanism of supercritical CO_2 on the chemical structure and composition of high-rank coals with different damage degrees. *Fuel* **2023**, 344, No. 128027.

(3) Ranathunga, A. S.; Perera, M. S. A.; Ranjith, P. G.; Zhang, X. G.; Wu, B. Super-critical carbon dioxide flow behaviour in low rank coal: A meso-scale experimental study. *J. CO_2 Util.* **2017**, 20, 1−13.

(4) Zhang, L.; Li, J. H.; Xue, J. H.; Zhang, C.; Fang, X. Q. Experimental studies on the changing characteristics of the gas flow capacity on bituminous coal in CO_2-ECBM and N_2-ECBM. *Fuel* **2021**, 291, No. 120115.

(5) Anggara, F.; Sasaki, K.; Sugai, Y. The correlation between coal swelling and permeability during CO_2 sequestration: A case study using Kushiro low rank coals. *Int. J. Coal Geol.* **2016**, 166, 62−70.

(6) Fang, H. H.; An, L.; Sang, S. X.; Gu, C. C.; Yang, J.; Li, L.; et al. Numerical analysis of permeability rebound and recovery evolution with THM multi-physical field models during CBM extraction in crushed soft coal with low permeability and its indicative significance to CO_2 geological sequestration. *Energy* **2023**, 262, No. 125395.

(7) Wang, H. Y.; Li, J. L.; Dong, Z. H. Z.; Fan, C.; Zhang, Y. W.; Chen, X. Effect of thermal damage on the pore-fracture system during coal spontaneous combustion. *Fuel* **2023**, 339, No. 127439.

(8) Jeong, S. R.; Park, J. H.; Lee, J. H.; Jeon, P. R.; Lee, C. H. Review of the adsorption equilibria of CO2, CH4, and their mixture on coals and shales at high pressures for enhanced CH4 recovery and CO2 sequestration. *Fluid Phase Equilib.* **2023**, 564, No. 113591.

(9) Wei, Y. B.; Li, J. Q.; Du, Y. J.; Lu, S. F.; Li, W. B.; Yang, J.; et al. Classification evaluation of gas shales based on high-pressure mercury injection: A case study on Wufeng and Longmaxi formations in southeast sichuan, China. *Energy Fuels* **2021**, 35 (11), 9382−9395.

(10) Elsayed, M.; El-Husseiny, A.; Kwak, H.; Hussaini, S. R.; Mahmoud, M. New technique for evaluating fracture geometry and preferential orientation using pulsed field gradient nuclear magnetic resonance. *SPE J.* **2021**, 26 (5), 2880−2893.

(11) Li, Z. B.; Ren, T.; Li, X. C.; Qiao, M.; Yang, X. H.; Tan, L. H.; Nie, B. Multi-scale pore fractal characteristics of differently ranked coal and its impact on gas adsorption. *Int. J. Min. Sci. Techno* **2023**, 33 (4), 389−401.

(12) Mathews, J. P.; Pone, J. D. N.; Mitchell, G. D.; Halleck, P. High-resolution X-ray computed tomography observations of the thermal drying of lump-sized subbituminous coal. *Fuel Process. Technol.* **2011**, 92 (1), 58−64.

(13) Fang, H. H.; Sang, S. X.; Du, Y.; Liu, H. H.; Xu, H. J. Visualization characterization of minerals touched by interconnected pores and fractures and its demineralization effect on coal permeability during CO_2-ECBM process based on X-ray CT data. *J. Nat. Gas Sci. Eng.* **2021**, 95, No. 104213.

(14) Fang, H. H.; Sang, S. X.; Liu, S. Q. Three-dimensional spatial structure of the macro-pores and flow simulation in anthracite coal based on X-ray mu-CT scanning data. *Pet. Sci.* **2020**, 17 (5), 1221−1236.

(15) Huo, B. J.; Jing, X. D.; He, A. P.; Fan, C. J. Hydraulic-mechanical coupling model with dual-porosity dual-permeability for anisotropy coal seams and its application in mine gas extraction. *Adv. Civ. Eng.* **2019**, 2019, No. 4534835.

(16) Asahina, D.; Pan, P. Z.; Sato, M.; Takeda, M.; Takahashi, M. Hydraulic and mechanical responses of porous sandstone during pore pressure-induced reactivation of fracture planes: an experimental study. *Rock Mech. Rock Eng.* **2019**, 52 (6), 1645−1656.

(17) Wu, M. Q.; Li, H. T.; Wang, L.; Yang, X. L.; Dai, C. Y.; Yang, N.; et al. CT quantitative assessment of the pore-fracture structures and permeability behaviors of long-flame coal treated by infrared rapid heating. *Energy* **2023**, 274, No. 127308.

(18) Zhu, Q. Z.; Wang, X. L.; Zuo, Y. Q.; Pan, J. N.; Ju, Y. W.; Su, X. F.; Yu, K. Numerical simulation of matrix swelling and its effects on fracture structure and permeability for a high-rank coal based on X-ray micro-CT image processing techniques. *Energy Fuels* **2020**, 34 (9), 10801−10809.

(19) Yoon, H.; Dewers, T. A. Nanopore structures, statistically representative elementary volumes, and transport properties of chalk. *Geophys. Res. Lett.* **2013**, 40 (16), 4294−4298.

(20) Fang, H. H.; Sang, S. X.; Liu, S. Q.; Liu, S. P. Experimental simulation of replacing and displacing CH_4 by injecting supercritical CO_2 and its geological significance. *Int. J. Greenhouse Gas Control* **2019**, 81, 115−125.

(21) Liu, W.; Han, D. Y.; Wang, G.; Chu, X. Y. Representative elementary volume evaluation of coal microstructure based on CT 3D reconstruction. *Fuel* **2023**, 336, No. 126965.

(22) Fang, H. H.; Sang, S. X.; Liu, S. Q.; Liu, H. H.; Xu, H. J.; Huang, Y. H. Determination of representative elementary volume of digital coal based on fractal theory with X-ray CT data and its application in fractal permeability predication model. *Front. Earth Sci.* **2022**, 16 (3), 657−670.

(23) Li, Z. W.; Zhang, G. Y. Fracture segmentation method based on contour evolution and gradient direction consistency in sequence of coal rock CT images. *Math. Probl. Eng.* **2019**, 2019, No. 2980747.

(24) Kumar, J.; Mendhe, V. A.; Kamble, A. D.; Bannerjee, M.; Mishra, S.; Singh, B. D.; Mishra, V. K.; Singh, P. K.; Singh, H. Coalbed methane reservoir characteristics of coal seams of south Karanpura coalfield, Jharkhand, India. *Int. J. Coal Geol.* **2018**, 196, 185−200.

(25) Lyu, S. F.; Chen, X. J.; Li, R.; Wang, S. W.; Liu, J.; Shen, P. L. Microstructure analysis on the fracture network in high-rank coals. *Earth Space Sci.* **2021**, 8 (8), No. e2021EA001780.

(26) Liu, H. P.; Rodrigues, S.; Shi, F. N.; Esterle, J.; Manlapig, E. Coal washability analysis using X-ray tomographic images for different lithotypes. *Fuel* **2017**, *209*, 162−171.

(27) Zhou, H. W.; Zhong, J. C.; Ren, W. G.; Wang, X. Y.; Yi, H. Y. Characterization of pore-fracture networks and their evolution at various measurement scales in coal samples using X-ray mu CT and a fractal method. *Int. J. Coal Geol.* **2018**, *189*, 35−49.

(28) Sun, L. L.; Zhang, C.; Wang, G.; Huang, Q. M.; Shi, Q. L. Research on the evolution of pore and fracture structures during spontaneous combustion of coal based on CT 3D reconstruction. *Energy* **2022**, *260*, No. 125033.

(29) Li, Z. T.; Liu, D. M.; Cai, Y. D.; Ranjith, P. G.; Yao, Y. B. Multi-scale quantitative characterization of 3-D pore-fracture networks in bituminous and anthracite coals using FIB-SEM tomography and X-ray mu-CT. *Fuel* **2017**, *209*, 43−53.

(30) Akhondzadeh, H.; Keshavarz, A.; Al-Yaseri, A. Z.; Ali, M.; Awan, F. U. R.; Wang, X.; Yang, Y. F.; Iglauer, S.; Lebedev, M. Pore-scale analysis of coal cleat network evolution through liquid nitrogen treatment: A Micro-Computed Tomography investigation. *Int. J. Coal Geol.* **2020**, *219*, No. 103370.

(31) Zhang, G. L.; Ranjith, P. G.; Perera, M. S. A.; Haque, A.; Choi, X.; Sampath, K. S. M. Characterization of coal porosity and permeability evolution by demineralisation using image processing techniques: A micro-computed tomography study. *J. Nat. Gas Sci. Eng.* **2018**, *56*, 384−396.

(32) Wang, M. F.; Wang, J. J.; Tao, S.; Tang, D. Z.; Wang, C. C.; Yi, J. Quantitative characterization of void and demineralization effect in coal based on dual-resolution X-ray computed tomography. *Fuel* **2020**, *267*, No. 116836.